applied optics

Autler–Townes splitting biosensing based on a nonuniform photonic crystal waveguide with feedback loop

GUOHUI YUAN, FANGCAO PENG, LEI GUAN, ZHENMING PENG, AND ZHUORAN WANG*

School of Information and Communication Engineering, University of Electronic Science and Technology of China, Chengdu 611731, China

**Corresponding author: wangzhuoran@uestc.edu.cn*

Received 6 June 2018; revised 24 July 2018; accepted 24 July 2018; posted 24 July 2018 (Doc. ID 334597); published 16 August 2018

Aimed at a high-performance biosensor for sensing biological molecules quickly and accurately, a novel nonuniform photonic crystal waveguide (NUPhCW) with a feedback loop is systematically investigated based on the mode-splitting effect. Thanks to the careful design of the nonuniform holes of NUPhCW with a feedback loop, the Autler–Townes splitting occurs in our device, and the spacing of two splitting resonance modes changes with the environmental refractive index, which is beneficial for achieving biosensing scenarios. Further, this integrated structure allows for self-referencing detection for immunity against environmental noise. Sensitivity of the NUPhCW is achieved at ~117 nm/RIU, which is 2.6 times more than that of the common microring resonator, indicating that our proposed device structure would be promising for high-quality optical label-free sensing.

OCIS codes: (280.1415) Biological sensing and sensors; (130.5296) Photonic crystal waveguides; (280.4788) Optical sensing and sensors; (230.3120) Integrated optics devices.

https://doi.org/10.1364/AO.57.006976

1. INTRODUCTION

Currently, optical biosensor technology is becoming a cutting-edge research topic, and various optical resonant cavities, such as microring resonators (MRRs) [1], surface plasmon resonators (SPRs) [2], and 1D photonic crystals (1D PhCs) [3], have been widely investigated for applications in clinical analysis, healthcare, and environmental monitoring as integrated optical label-free biosensors [4].

MRRs and 1D PhCs have been employed for biosensing applications due to their unique features such as ultrahigh quality factor (Q factor), extremely small mode volume, and compact footprint as well as being integrated with conventional waveguides [5,6]. In 2007, Vos *et al.* [1] proposed a label-free biosensor based on MRRs with a radius of 5 μm, which exhibited bulk detection sensitivity of ~70 nm/RIU. In 2010, Iqbal *et al.* [7] experimentally demonstrated a sensing array based on silicon MRRs and showed a bulk refractive index sensitivity of ~163 nm/RIU. In 2016, Yan *et al.* [8] fabricated an MRR with a radius of 10 μm, achieving the measured bulk sensitivity ~44.6 nm/RIU. In 2017, Lo *et al.* [9] fabricated an MRR with a radius of ~7 μm, achieving a bulk index sensitivity of ~111 nm/RIU.

In terms of 1D PhCs, in 2013, Quan *et al.* [10] reported a label-free sensor using 1D PhCs that had a sensitivity of ~83 nm/RIU. In 2016, Yang *et al.* [11] proposed a novel multiplexed ultracompact high-sensitivity 1D PhC sensor array and presented a concept model with three parallel channels achieving the bulk refractive index sensitivities of 112.6 nm/RIU, 121.7 nm/RIU, and 148.5 nm/RIU, respectively. In 2017, Sun *et al.* [12] proposed an ultracompact air-mode 1D PhC, which possessed a high sensitivity of 252 nm/RIU.

To a certain extent, the sensing performance of these biosensor platforms using symmetric single-resonance peak shifts arising from the change of the refractive index is limited. Thus, in order to improve the sensing performance, many effects either to modify the biosensors themselves or to integrate different structures to achieve a Vernier effect [13], mode-splitting [14], Fano-resonance effect [15], electromagnetically induced transparency (EIT) [16], and so on have been made in optical biosensor areas in the past years.

EIT, produced by the quantum interference effect in an interaction system, forms a sharp transparency window in an interaction system, which has been applied to various scenarios, such as slow light [17], nonlinear effects [18], optical switching [19], optical biosensors [20], and so on. There is a similar phenomenon to EIT called Autler–Townes splitting (ATS) [21], which is formed by mode splitting due to the field-driven interactions leading to energy-level splitting. In biological sensing, the variation of the spacing between two splitting resonance modes of ATS with the environmental refractive index can be used for an optical label-free biosensor. Using its two splitting modes, the ATS is ideally suitable for sensing applications because it enables a self-referencing detection system that is immune to environmental noise [14,22,23]. Particularly, whispering-gallery-mode microresonators (WGMRs) have been excellent and fruitful platforms to form EIT and ATS. To achieve the ATS for label-free sensing, structures based on WGMRs have been widely investigated [24–33]. The MRR integrated with a 1D PhC structure can maintain the compact footprint of MRR and further improve its performances [9,15,34]. However, ATS biosensing based on an MRR integrated with a 1D PhC structure has, thus far, not yet been demonstrated.

The main purpose of this manuscript is to explore an on-chip device with the ATS characteristics for high-performance biosensors. The concept of a ring resonator is borrowed by introducing a feedback loop to the novel nonuniform photonic crystal waveguide (NUPhCW) to form an equivalent circular cavity. Our investigations show that the sensitivity of this sensor is improved greatly than that of a common microring resonator. On the other hand, in order to introduce the optical power into the feedback loop, the reflection of 1D PhCs has to be reduced slightly and, accordingly, lower the sensitivity of our device compared with that of 1D PhCs. However, this integrated structure allows self-referencing detection that is immune to environmental noise [14,22,23], which is quite attractive for the realization of a robust and stable biosensor. Furthermore, the device is based on a silicon-on-insulator (SOI) platform compatible with the CMOS process, allowing for a strong reduction of the chip cost by utilizing high volume manufacturing. Thus, this sensor has great potential for specific biological molecular detection.

2. DESIGN PRINCIPLES OF NUPhCW

We use the FDTD method to investigate the design principles of NUPhCW in a water environment. As show in Fig. 1, NUPhCW is composed of $2N_0 - 1$ holes with the reduced radii from the center to the two sides (region II) and $2N$ uniform holes in regions I and III, periodically etched into a 0.45 μm width silicon ridge waveguide. In order to achieve a Gaussian-type attenuation, the radii of nonuniform holes are parabolically tapered from the center to both sides, as expressed in Eq. (1):

$$r_i = r_{\text{center}} + (r_{\text{end}} - r_{\text{center}})\left(\frac{i-1}{N_0-1}\right)^2 \qquad i = 1, 2, \ldots, N_0, \tag{1}$$

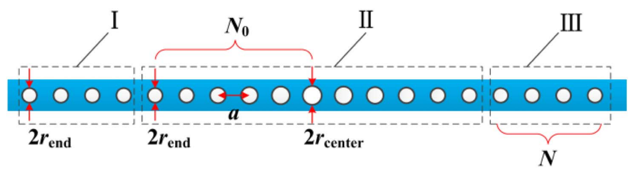

Fig. 1. Schematic of the NUPhCW.

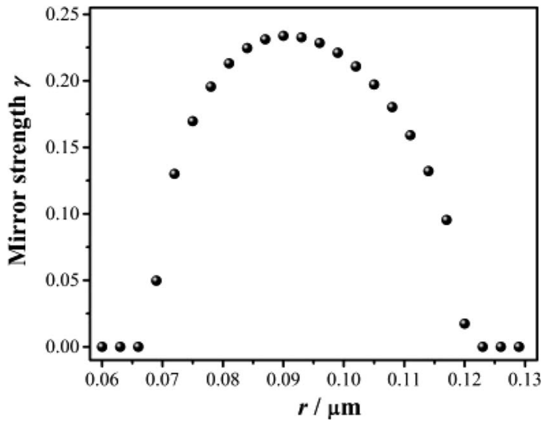

Fig. 2. Mirror strength γ for different hole radii.

where r_i is the radius of the ith hole from the center hole, and the radii of the center hole and the last nonuniform hole on both sides are r_{center} and r_{end}, respectively.

The main structural parameters are the hole period a, N, N_0, r_{center}, and r_{end}, which are the keys of our structural design. First, the period a is determined as $\lambda_0/2n_{\text{eff}}$ [35], where the effective index of the NUPhCW cavity n_{eff} is estimated to 2.63 by our numerical modeling of the strip waveguide. The resonant wavelength λ_0 is chosen to be 1.677 μm, so the period a can be calculated to 0.315 μm. Then, r_{end} is chosen to realize the maximal mirror strength γ, as shown in Fig. 2, which shows the calculated mirror strength γ for different hole radii. γ can be calculated by

$$\gamma = \sqrt{\left(\frac{\omega_2 - \omega_1}{\omega_2 + \omega_1}\right)^2 - \left(\frac{\omega_r - \omega_0}{\omega_0}\right)^2}, \tag{2}$$

where ω_2, ω_1, ω_0, and ω_r are the air band edge, dielectric band edge, midgap frequency, and cavity resonance frequency, respectively [36]. From the perspective of γ, the optimal r_{end} is 0.092 μm to maximize the reflection, and the optimal r_{center} of 0.125 μm is chosen to minimize the reflection.

3. NUPHCW WITH FEEDBACK LOOP (NUPhCW-FL)

To calculate and observe the variation of Q and ER of the NUPhCW cavity, FDTD is used to determine N_0 and N, as shown in Figs. 3(a) and 3(b). The grid step size used in FDTD simulations was 20 nm. The optimal Q and ER can be obtained as N and N_0 are chosen at 4 and 6, respectively. Furthermore, fine-tuning r_{center} to 0.092 μm and r_{end} to 0.125 μm can further maximize Q and ER, as shown in Figs. 3(c) and 3(d). Finally, the geometrical parameters of NUPhCW cavity are determined and summarized in Table 1.

Introducing a feedback loop to our optimized NUPhCW would form a microring resonator (MRR) further, and the illustration of our proposed NUPhCW with feedback loop (NUPhCW-FL) device is shown in Fig. 4. The width of access waveguide W_b of 0.39 μm is to satisfy the mode matching for the coupling process between the access waveguide and NUPhCW-FL. Actually, the proposed device can be equivalent

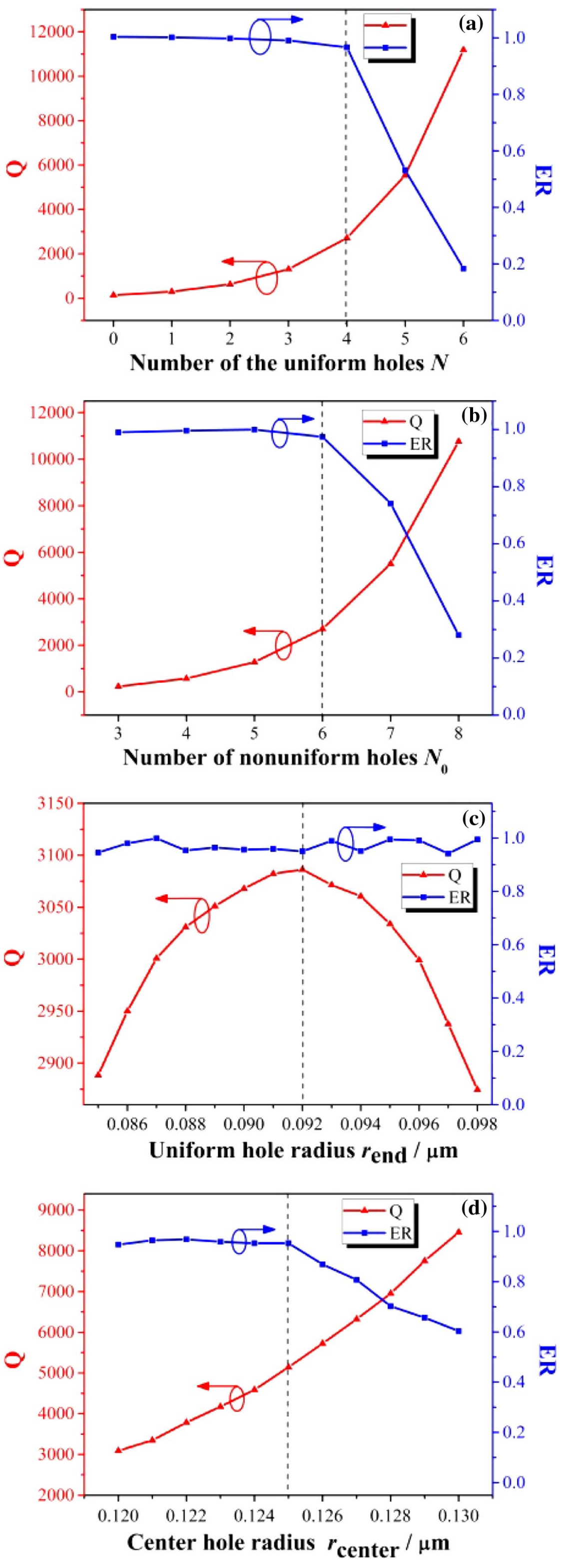

Fig. 3. (a) Variations of Q and ER with N on the condition of $a = 0.315$ μm, $N_0 = 5$, $r_{center} = 0.125$ μm, and $r_{end} = 0.09$ μm. (b) Variations of Q and ER with N_0 on the condition of $a = 0.315$ μm, $N = 4$, $r_{center} = 0.125$ μm, and $r_{end} = 0.092$ μm. (c) Variations of Q and ER with r_{end} on the condition of $a = 0.315$ μm, $N = 4$, $N_0 = 6$, and $r_{center} = 0.125$ μm. (d) Variations of Q and ER with r_{center} on the condition of $a = 0.315$ μm, $N = 4$, $N_0 = 6$, and $r_{end} = 0.092$ μm.

Table 1. Designed Structural Parameters of the NUPhCW

Parameter	Numerical Value
Waveguide Width (W)	0.45 μm
Hole Periodicity (a)	0.315 μm
Number of Nonuniform Holes (N_0)	6
Number of Uniform Holes (N)	4
Uniform Holes (r_{end})	0.092 μm
Central Hole Radius (r_{center})	0.125 μm

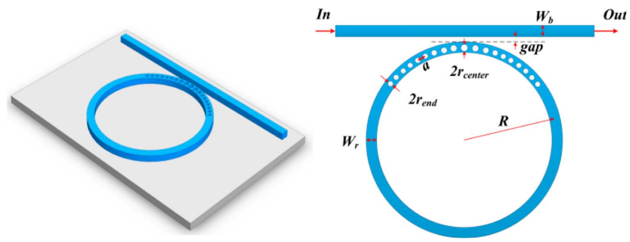

(a) (b)

Fig. 4. (a) Illustration of NUPhCW-FL. (b) Key geometrical parameters of NUPhCW-FL.

to two resonators, i.e., NUPhCW and MRR, as illustrated in Fig. 5, and the resonance wavelengths of NUPhCW and MRR are λ_{NUPhCW} and λ_{MRR}, respectively.

When the light launches into the in port of the access waveguide, the resonance mode splitting (ATS) occurs, which can be detected from the out port due to the introduction of feedback loop to NUPhCW.

The formation of ATS (that is, the mode splits into two modes) needs strong inter-resonator coupling between NUPhCW and MRR and satisfies the certain relationship between Q factors of two interacting modes as well [31], which means two Q factors would be close to each other.

First, K is defined as

$$K = \frac{P_{out}}{P_{in}}, \tag{3}$$

where P_{in} is the input light power and P_{out} is the output light power from NUPhCW, as shown in Fig. 5(a). P_{out} indicates

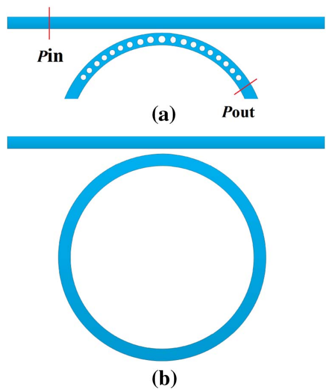

Fig. 5. Illustration of two resonator cavities: (a) NUPhCW; (b) MRR.

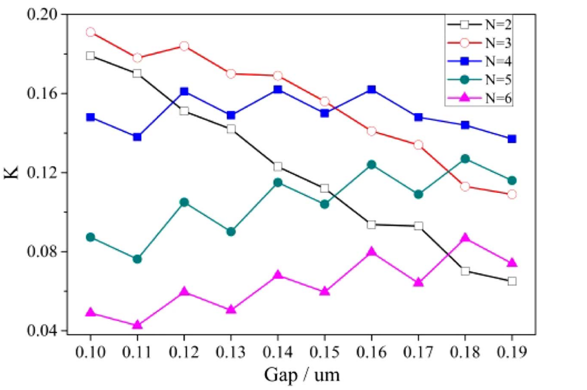

Fig. 6. Variation of K with gap in different N.

the optical power coupling into MRR from the NUPhCW; thus, K indicates, indirectly, the inter-resonator coupling strength between the NUPhCW and the MRR. As shown in Fig. 5, the inter-resonator coupling strength can be controlled by adjusting the mirror reflection ratio of the NUPhCW, which is related to N. Figure 6 shows K calculated by FDTD, and it is observed that, when N is less than or equal to 3, K drastically decreases with the increase of gap. However, when N equals to 4 or is greater than 4, K does not change much with the increase of gap, Furthermore, the greater K is obtained with the increase of N when N equals to 4 or is greater than 4. Thus, in order to obtain stronger inter-resonator coupling, N is determined to 4.

Second, to satisfy the certain relationship between Q factors of two interacting modes, Q_{NUPhCW} of the NUPhCW is important. As shown in Fig. 5(a), Q_{NUPhCW} and ER_{NUPhCW} of the NUPhCW are influenced by N. Figure 7 shows the variations of Q_{NUPhCW} and ER_{NUPhCW} with a gap in different N. It is observed that Q_{NUPhCW} increases with the increase of gap and N, and ER_{NUPhCW} decreases with the increase of gap and increases with the increase of N. Thus, in order to achieve greater ER_{NUPhCW} and maintain high Q_{NUPhCW}, which is close to the Q factor of the interacting mode of the MRR, the gap of 0.14 μm can be determined, in which the respective Q factor of

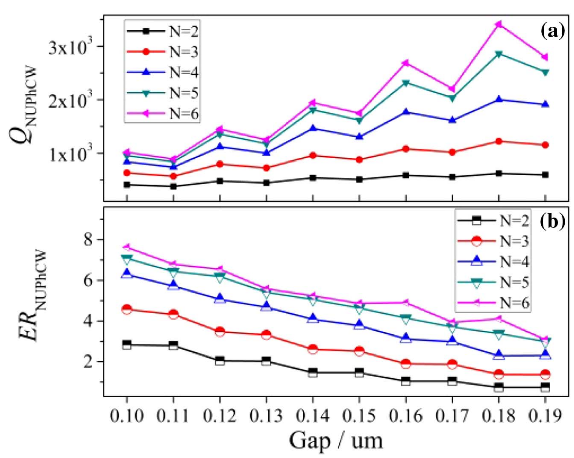

Fig. 7. (a) Variation of Q_{NUPhCW} with gap in different N. (b) Variation of ER_{NUPhCW} with gap in different N.

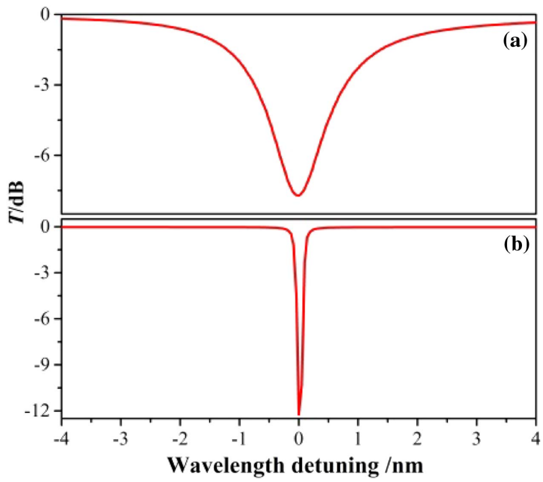

Fig. 8. (a) Resonance spectrum of the NUPhCW. (b) Resonance spectrum of the MRR.

NUPhCW and MRR is 1.482×10^3 and 1.346×10^4 calculated by the FDTD method, and $Q_{\mathrm{MRR}}/Q_{\mathrm{NUPhCW}}$ is around 9.

According to the above structural parameters, the transmission spectrum of the NUPhCW-FL is simulated by FDTD, when we tune and make the resonance wavelengths equal ($\lambda_{\mathrm{NUPhCW}} = \lambda_{\mathrm{MRR}}$) indicating zero wavelength detuning, as shown in Fig. 8, and the resonance mode of the NUPhCW-FL splits into two modes of λ_1 and λ_2, and the distance of two modes $\Delta\lambda$ is $\lambda_2 - \lambda_1$, as shown in Fig. 9. The transmission spectrum of the NUPhCW-FL forms a symmetric doublet shape, i.e., ATS. In order to achieve this purpose, we change the radius R of the MRR because the resonant wavelength of the MRR changes with R, and the resonant wavelength of the NUPhCW is not changed basically. Thus, we achieve zero wavelength detuning in the proposed device when R is 5.001 μm. Thus, depending on the similar Q factors of the interacting modes and their strong coupling, the ATS in our proposed device can be realized.

To investigate sensing properties, the NUPhCW-FL is supposed to be immersed in a solution containing the bio-analytes, and the sensing characteristics of the NUPhCW-FL are investigated by monitoring the change ($\delta\lambda_{\mathrm{ATS}}$) of spectral distance $\Delta\lambda$ with the refractive index of the surrounding environment as

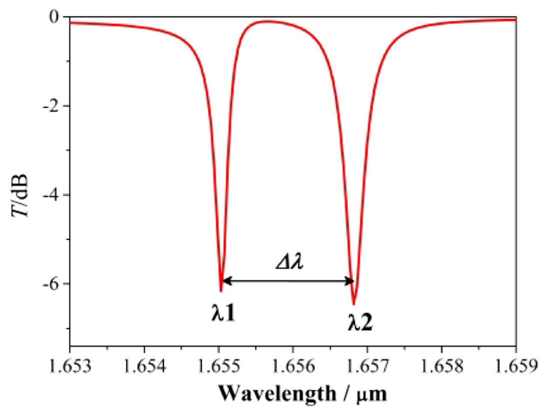

Fig. 9. Transmission spectrum of the NUPhCW-FL.

Table 2. Relationship Between $\delta\lambda_{ATS}$ and Δn

n	Δn (RIU)	λ_1 (nm)	λ_2 (nm)	$\Delta\lambda$ (nm)	$\delta\lambda_{ATS}$ (nm)
1.33	0	1655.03	1656.82	1.79	0
1.34	0.01	1655.81	1658.24	2.43	0.64
1.35	0.02	1656.40	1659.89	3.49	1.70
1.36	0.03	1656.91	1661.54	4.63	2.84
1.37	0.04	1657.41	1663.25	5.84	4.05
1.38	0.05	1657.91	1665.00	7.09	5.30

listed in Table 2. The transmission spectra of the NUPhCW-FL are monitored in Fig. 10, with the variation of the refractive index of environmental medium from $n = 1.33$ to $n = 1.38$. The refractive index of silicon is 3.476, and the refractive index of substrate material (silica) is assumed to be 1.444. In Fig. 9 or the top one of Fig. 10 ($n = 1.33$), it is observed that the splitting resonances become symmetric with the same linewidths and depths when zero-detuning is achieved. Q factors of the left and right peaks are $\sim 1 \times 10^4$. As shown in Fig. 10, when the refractive index of the environmental medium increases from 1.34 to 1.38, $\Delta\lambda$ is wider, and the transmission also exhibits asymmetric splitting resonances (i.e., asymmetric ATS) resulting in unequal transmission dips because the resonant frequency between MRR and NUPhCW changes with the refractive index of environmental medium n [31]. The resonances are redshifted, but they have different shift rates. The linewidth of the left dip decreases slowly, and the linewidth of the right dip increases slowly with the increase of the refractive index. The Q factor of the left increases gradually to $\sim 2.3 \times 10^4$, and the Q factor of the right peak keeps to $\sim 1 \times 10^4$. Meanwhile, depth of the left dip decreases and depth of the right dip remains unchanged.

The sensitivity of the NUPhCW-FL can be estimated by

$$S = \frac{\delta\lambda}{\Delta n}, \tag{4}$$

where $\delta\lambda$ is the variation of the spectral distance $\Delta\lambda$, and Δn is the variation of the environmental refractive index. Thus, the sensitivity curve of the NUPhCW-FL is obtained by fitting

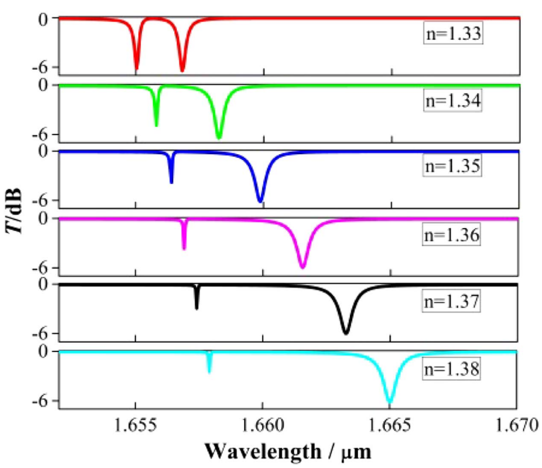

Fig. 10. Transmission spectra of the NUPhCW-FL when the refractive index of environmental medium n changes from $n = 1.33$ to $n = 1.38$.

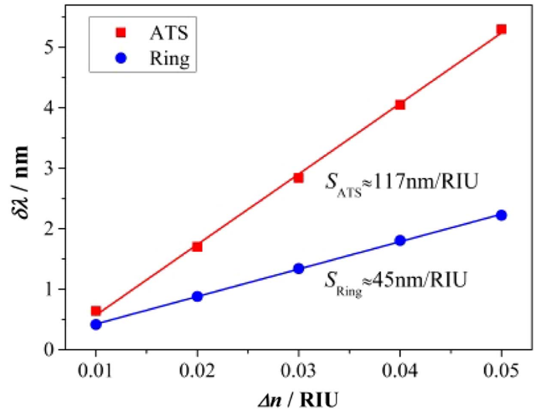

Fig. 11. Sensitivity fitting curve of the NUPhCW-FL and the common MRR, representing the variation of the spectral distance $\delta\lambda$ as a function of increasing n.

the $\delta\lambda_{ATS}$ and Δn, as shown in Fig. 11, and the sensitivity of the NUPhCW-FL S_{ATS} is ~ 117 nm/RIU.

As a comparison, the sensitivity fitting curve of the regular MRR with the same radius of our proposed device is also calculated and shown in Fig. 11, and the sensitivity S_{MRR} is ~ 45 nm/RIU. Thus, the sensing performance of the proposed device is greatly enhanced.

To calculate the largest refractive index change that can be detected, two splitting modes have to be observed simultaneously. In Fig. 10, depth of the left dip decreases, and depth of the right dip remains unchanged with the increase of the refractive index. In the actual experiment, the left dip will not be detected under the noise floor of the measurement system. Therefore, the largest refractive index change (i.e., the detection range) of this device is limited by the noise of the whole system. However, the system noise is ignored in our simulation. Thus, we have to wait for the left dip to disappear, where the refractive index is equal to ~ 1.43, so the detection range of the refractive index is estimated from 1.33 to 1.43.

4. CONCLUSION

We demonstrate a novel high-performance NUPhCW-FL biosensor with ATS owing to the mode interacting between the NUPhCW and the equivalent MRR. Further, the spectral spacing of ATS changes with the environmental refractive index, which can be utilized for an optical label-free biosensor. Also, the numerical simulation results by using FDTD show that the sensitivity of the NUPhCW-FL is ~ 117 nm/RIU, which is 2.6 times over the regular MRR. By using the NUPhCW-FL structure, the footprint of our device will not change compared with the MRR device, though the optical grating structures are integrated to the ring waveguide, which also simplifies this kind of coupled-resonator device design. Furthermore, even if the absolute value of sensitivity is not high, and a little increased complexity is introduced, our design still enhances the performance several times, which can also offer benefits and new ideas not only for ring resonators but also for other optical biosensors. Thus, we believe that NUPhCW-FL has potential for biological and chemical analysis scenarios.

Funding. National Natural Science Foundation of China (NSFC) (61575038, 61571096, 61775030); Fundamental Research Funds for the Central Universities (ZYGX2015J052); Key Laboratory Fund of Beam Control Chinese Academy of Sciences (CAS) (2017LBC003).

REFERENCES

1. K. D. Vos, I. Bartolozzi, E. Schacht, P. Bienstman, and R. Baets, "Silicon-on-insulator microring resonator for sensitive and label-free biosensing," Opt. Express **15**, 7610–7615 (2007).
2. B. Wu and Q. Wang, "Design optimization of highly sensitive LSPR enhanced surface plasmon resonance biosensors with nanoholes," Chin. Opt. Lett. **6**, 323–326 (2008).
3. M. T. Yaseen, Y. Yang, M. H. Shih, and Y. Chang, "Optimization of high-Q coupled nanobeam cavity for label-free sensing," Sensors **15**, 25868–25881 (2015).
4. Z. Wang, L. Guan, Y. Chen, L. Dong, and G. Yuan, "Single-waveguide-based microresonators for optical sensing," Chin. Opt. Lett. **15**, 010006 (2017).
5. P. Yu, B. Qi, X. Jiang, M. Wang, and J. Yang, "Ultrasmall-V high-Q photonic crystal nanobeam microcavities based on slot and hollow-core waveguides," Opt. Lett. **36**, 1314–1316 (2011).
6. K. J. Vahala, "Optical microcavities," Nature **424**, 839–846 (2003).
7. M. Iqbal, M. A. Gleeson, B. Spaugh, F. Tybor, W. G. Gunn, M. Hochberg, T. Baehr-Jones, R. C. Bailey, and L. C. Gunn, "Label-free biosensor array based on silicon ring resonators and high-speed optical scanning instrumentation," IEEE J. Sel. Top. Quantum Electron. **16**, 654–661 (2010).
8. H. Yan, L. Huang, X. Xu, S. Chakravarty, N. Tang, H. Tian, and R. T. Chen, "Unique surface sensing property and enhanced sensitivity in microring resonator biosensors based on subwavelength grating waveguides," Opt. Express **24**, 29724–29733 (2016).
9. S. M. Lo, S. Hu, G. Gaur, Y. Kostoulas, S. M. Weiss, and P. M. Fauchet, "Photonic crystal microring resonator for label-free biosensing," Opt. Express **25**, 7046–7054 (2017).
10. Q. Quan, D. L. Floyd, I. B. Burgess, P. B. Deotare, I. W. Frank, S. K. Y. Tang, R. Ilic, and M. Loncar, "Single particle detection in CMOS compatible photonic crystal nanobeam cavities," Opt. Express **21**, 32225–32233 (2013).
11. D. Yang, C. Wang, and Y. Ji, "Silicon on-chip 1D photonic crystal nanobeam bandstop filters for the parallel multiplexing of ultra-compact integrated sensor array," Opt. Express **24**, 16267–16279 (2016).
12. F. Sun, Z. Fu, C. Wang, Z. Ding, C. Wang, and H. Tian, "Ultra-compact air-mode photonic crystal nanobeam cavity integrated with bandstop filter for refractive index sensing," Appl. Opt. **56**, 4363–4368 (2017).
13. B. Troia, F. D. Leonardis, and V. M. N. Passaro, "Cascaded ring resonator and Mach-Zehnder interferometer with a sagnac loop for Vernier-effect refractive index sensing," Sens. Actuators B Chem. **240**, 76–89 (2017).
14. J. Zhu, S. K. Ozdemir, Y. Xiao, L. Li, L. He, D. Chen, and L. Yang, "On-chip single nanoparticle detection and sizing by mode splitting in an ultrahigh-Q microresonator," Nat. Photonics **4**, 46–49 (2010).
15. F. Peng, Z. Wang, L. Guan, G. Yuan, and Z. Peng, "High sensitivity refractive index sensing based on fano resonances in a photonic crystal cavity-coupled microring resonator," IEEE Photon. J. **10**, 6600808 (2018).
16. K. Boller, A. Imamolu, and S. E. Harris, "Observation of electromagnetically induced transparency," Phys. Rev. Lett. **66**, 2593–2596 (1991).
17. C. Jiang, H. Liu, Y. Cui, X. Li, and B. Chen, "Electromagnetically induced transparency and slow light in two-mode optomechanics," Opt. Express **21**, 12165–12173 (2013).
18. X. Yan, L. Wang, B. Yin, and J. Song, "Electromagnetically induced transparency and enhanced self-Kerr nonlinearity in a four-level scheme," Optik **122**, 986–990 (2011).
19. A. Dantan, M. Albert, and M. Drewsen, "Cavity electromagnetically induced transparency, and optical switching with ion Coulomb crystals," in *Conference on Lasers and Electro-Optics Europe and 12th European Quantum Electronics Conference* (2011).
20. H. Wanare and J. Jose, "Bio-organism detection in one-dimensional photonic crystals using electromagnetically induced transparency," Opt. Lett. **37**, 410–412 (2012).
21. P. M. Anisimov, J. P. Dowling, and B. C. Sanders, "Objectively discerning Autler-Townes splitting from electromagnetically induced transparency," Phys. Rev. Lett. **107**, 163604 (2011).
22. S. I. Shopova, Y. Sun, A. T. Rosenberger, and X. Fan, "Highly sensitive tuning of coupled optical ring resonators by microfluidics," Microfluid. Nanofluid. **6**, 425–429 (2009).
23. M. Li, X. Wu, L. Liu, X. Fan, and L. Xu, "Self-referencing optofluidic ring resonator sensor for highly sensitive biomolecular detection," Anal. Chem. **85**, 9328–9332 (2013).
24. C. E. Campanella, F. D. Leonardis, L. Mastronardi, P. Malara, G. Gagliardi, and V. M. N. Passaro, "Investigation of refractive index sensing based on Fano resonance in fiber Bragg grating ring resonators," Opt. Express **23**, 14301–14313 (2015).
25. K. McGarvey-Lechable and P. Bianucci, "Maximizing slow-light enhancement in one-dimensional photonic crystal ring resonators," Opt. Express **22**, 26032–26041 (2014).
26. J. Čtyroký, I. Richter, and M. Šiňor, "Dual resonance in a waveguide-coupled ring microresonator," Opt. Quantum Electron. **38**, 781–797 (2006).
27. P. Malara, L. Mastronardi, C. E. Campanella, A. Giorgini, S. Avino, V. M. N. Passaro, and G. Gagliardi, "A split-mode fiber Bragg-grating sensor for high-resolution static strain measurements," Opt. Lett. **39**, 6899–6902 (2014).
28. C. E. Campanella, C. M. Campanella, F. De Leonardis, and V. M. N. Passaro, "A high efficiency label-free photonic biosensor based on vertically stacked ring resonators," Eur. Phys. J. Spec. Top. **223**, 2009–2021 (2014).
29. F. De Leonardis, C. E. Campanella, B. Troia, A. G. Perri, and V. M. N. Passaro, "Performance of SOI Bragg grating ring resonator for nonlinear sensing applications," Sensors **14**, 16017–16034 (2014).
30. C. E. Campanella, L. Mastronardi, F. De Leonardis, P. Malara, G. Gagliardi, and V. M. N. Passaro, "Investigation of fiber Bragg grating based mode-splitting resonant sensors," Opt. Express **22**, 25371–25384 (2014).
31. B. Peng, S. K. Özdemir, W. Chen, F. Nori, and L. Yang, "What is and what is not electromagnetically induced transparency in whispering-gallery microcavities," Nat. Commun. **5**, 5082 (2014).
32. G. Gao, D. Li, Y. Zhang, S. Yuan, and A. Armghan, "Tuning of resonance spacing over whole free spectral range based on Autler-Townes splitting in a single microring resonator," Opt. Express **23**, 26895–26904 (2015).
33. L. Bo, P. H. Chong, and C. Lee, "Tunable Autler-Townes splitting observation in coupled whispering gallery mode resonators," IEEE Photon. J. **8**, 1–10 (2016).
34. J. Y. Lee and P. M. Fauchet, "Slow-light dispersion in periodically patterned silicon microring resonators," Opt. Lett. **37**, 58–60 (2012).
35. Q. Quan and M. Loncar, "Deterministic design of wavelength scale, ultra-high Q photonic crystal nanobeam cavities," Opt. Express **19**, 18529–18542 (2011).
36. D. Yang, P. Zhang, H. Tian, Y. Ji, and Q. Quan, "Ultrahigh-Q and low-mode-volume parabolic radius-modulated single photonic crystal slot nanobeam cavity for high-sensitivity refractive index sensing," IEEE Photon. J. **7**, C1-1486 (2017).